



Article

Synthesis and Electrochemical Properties of Bi_2MoO_6 /Carbon Anode for Lithium-Ion Battery Application

Tingting Zhang ¹, Emilia Olsson ² , Mohammadmehdi Choolaei ², Vlad Stolojan ³ ,
Chuanqi Feng ^{1,2,*}, Huimin Wu ¹, Shiquan Wang ¹ and Qiong Cai ^{2,*} 

¹ Hubei Collaborative Innovation Center for Advanced Organic Chemical Materials and Ministry of Education Key Laboratory for Synthesis and Applications of Organic Functional Molecules, Hubei University, Wuhan 430062, China; zhangtingting@iccas.ac.cn (T.Z.); whm267@126.com (H.W.); wsqhao@hubu.edu.cn (S.W.)

² Department of Chemical and Process Engineering, Faculty of Engineering and Physical Sciences, University of Surrey, Guildford GU2 7XH, UK; k.olsson@surrey.ac.uk (E.O.); m.choolaei@surrey.ac.uk (M.C.)

³ Advanced Technology Institute, Department of Electrical and Electronic Engineering, Faculty of Engineering and Physical Sciences, University of Surrey, Guildford GU2 7XH, UK; V.Stolojan@surrey.ac.uk

* Correspondence: cfeng@hubu.edu.cn (C.F.); q.cai@surrey.ac.uk (Q.C.)

Received: 16 December 2019; Accepted: 29 February 2020; Published: 4 March 2020



Abstract: High capacity electrode materials are the key for high energy density Li-ion batteries (LIB) to meet the requirement of the increased driving range of electric vehicles. Here we report the synthesis of a novel anode material, Bi_2MoO_6 /palm-carbon composite, via a simple hydrothermal method. The composite shows higher reversible capacity and better cycling performance, compared to pure Bi_2MoO_6 . In 0–3 V, a potential window of 100 mA/g current density, the LIB cells based on Bi_2MoO_6 /palm-carbon composite show retention reversible capacity of 664 mAh·g⁻¹ after 200 cycles. Electrochemical testing and *ab initio* density functional theory calculations are used to study the fundamental mechanism of Li ion incorporation into the materials. These studies confirm that Li ions incorporate into Bi_2MoO_6 via insertion to the interstitial sites in the MoO_6 -layer, and the presence of palm-carbon improves the electronic conductivity, and thus enhanced the performance of the composite materials.

Keywords: Li ion batteries; composite; electrode materials; hydrothermal synthesis; electrochemical performance; *ab initio* calculations

1. Introduction

Lithium-ion batteries (LIBs) are ubiquitous in electric vehicles, laptops, mobile phones and various electronic products for energy storage, due to their high energy density, good electronic performance, low self-discharge and long cycle life [1–3]. The properties of the electrode and electrolyte materials determine the electrochemical performance of a LIB cell, and thus have been researched widely. Negative electrode (i.e., anode) materials with low operating potentials (close to 0 V_{Li} (Li⁺/Li)) and high storage capacity are important for achieving high LIB battery performance, as the overall cell voltage is determined by the difference between the positive electrode and the negative electrode. Commercial LIBs normally utilize a graphite anode which operates at 0.1 V_{Li} with good stability in conventional liquid carbonate electrolytes and give a specific capacity of 372 mAh·g⁻¹ [4–8]. To further increase the driving range of electric vehicles and the lifetime of portable electronics between charge and discharge, we need to have much higher capacity—at least double the capacity of graphite anodes used in LIBs. Thus, there has been development of new anode materials. Lithium metal has been considered as a

promising anode material for LIBs owing to its ultra-high theoretical capacity (3860 mAh g^{-1}) [9], but face significant challenges in the uncontrolled dendrite formation and the associated huge performance degradation. Although the promise of Li metal anode has attracted a lot of research interests, with considerable advances being made into understanding the failure mechanisms and various strategies to mitigate the Li dendrite formation, it is still far from practical utilizations in commercial LIBs [9–11]. The alloy anode materials such as tin and silicon show high specific capacity ($1000\text{--}4000 \text{ mAh}\cdot\text{g}^{-1}$) and low working voltage ($0.1\text{--}1.0 V_{\text{Li}}$). However, the expansion of volume (as much as 400%) and the consequent irreversible morphological and mechanical changes lead to a significant decrease of capacity during the alloy reaction, which prohibit the development of commercial products. Although recent advances in nanostructure, carbon coating and Si/Sn based composite have improved the stability and the electrochemical performance of the anode materials, further development is still needed [5,7,8,12]. Conversion type transition metal oxides (such as oxides of iron, manganese, cobalt, copper and nickel) [13] show high specific capacities and high rate capabilities, and have attracted increased attention. However, low electrical conductivity [14] and the fragility of the electrode limit their development and wider use in practical applications [3,5–8].

Both binary oxides (MO_x , $M = \text{Ti, Mn, Sn, Fe, Co, Mo, Ni}$ and Cu , etc.) [14–16] and ternary oxides (ABO_x $A = \text{Ca, Mg, Bi, Ti, Zn, Fe, V, Mn, Co, Ni, Cu}$; $B = \text{Mn, Mo, Co, Fe, Ni, Ti, Nb, Cu, Sn}$; $A \neq B$.) [17–24] based on different reaction mechanisms (e.g., intercalation, conversion, and alloy reactions) have been proposed as electrode materials. Ternary oxides are more versatile, with a great number of possible combinations of metal A and B. ABO_x with nanostructure are advantageous as they have a high specific surface area, as well as a shorter diffusion path for Li ion than their micro-sized or bulk counterparts. However, most of the nano-sized materials exhibit rapid capacity degradation due to the inherent nature of low conductivity and aggregation over cycling [13–16]. To increase the electrochemical performance of metal oxides as battery electrodes, various approaches have been investigated, including: (1) minimizing particle size and optimizing particle shape, thickness, and nanostructure self-assembly [8,17], (2) fabricating hierarchically porous structures [25] in order to enhance the buffer space and active sites of electrochemical reaction which improve the rate capability and cycling stability of batteries, (3) combining hybrid metal oxides with large surface area and fast electron transport materials [26], in which case, various carbon materials have been studied for their high surface area, proper morphology and structures, and excellent electron transfer properties [12,27]. Porous carbonaceous materials [12,27] with tunable porosities, including activated carbon, ordered mesoporous carbons, carbon aerogels and graphene-based materials, have been widely used in the field of electrode materials in batteries. Carbon materials derived from biomass have drawn much interest, as they are sustainable, low cost, and give excellent properties such as high specific surface area, well-developed porous structure, high electrical conductivity, and electrochemical stability [27,28].

Many molybdenum based oxides were widely used as anode materials because of their high specific capacity, multiple valance states of oxides and high mass density which increased the capacity of the electrode materials. Many Mo based oxides, such as binary oxides (MoO_3 , MoO_2), ternary oxides (CaMoO_4 , MMoO_4 , $M = \text{Ni, Co, Mn}$) and CoMoO_4 were investigated as anode materials for LIBs [20–24]. However, unfortunately, complex preparation methods hinder their commercial application. Metal molybdates, particularly bismuth molybdate (Bi_2MoO_6), which is a conventional layered metal molybdate consisting of $[\text{Bi}_2\text{O}_2]^+$ layers sandwiched between $[\text{MO}_4]^{2-}$ slabs, could be used as potential LIB anode materials. The limited research on Bi_2MoO_6 as LIB anode shows that Bi_2MoO_6 has a much higher storage capacity than graphite, with initial charge capacity of over $900 \text{ mAh}\cdot\text{g}^{-1}$ reported [25,26], and can be considered as a promising material for an LIB anode. However, in the reported work [25,26,29–31], complicated processes and expensive materials (such as graphene and Ni foam) have been taken to synthesize Bi_2MoO_6 based materials, which are expensive and not suitable for large scale practical applications. Based on previous experience with metal oxides [14–19], the electrochemical performance of Bi_2MoO_6 could be improved by hybridizing Bi_2MoO_6 with cheap carbon materials, using simpler and cost-effective synthesis methods.

In this paper, we report our work on the development of Bi_2MoO_6 hybridized with carbon as LIB anode materials, via a simple hydrothermal route. The carbon material in this paper is synthesized from palm tree leaves, and is hereafter referred to as palm carbon. Palm carbon is chosen because it is easy to obtain, it shows a high electronic conductivity and is derived from a more sustainable source than other carbon materials, such as graphene and those derived from polymers. The prepared materials are characterized using a range of techniques including XRD, SEM, STEM (Scanning Transmission Electron Microscopy), Raman and XPS to understand the morphology and chemical properties. Density functional theory (DFT) calculations are also performed to gain insights into the structure of Bi_2MoO_6 and Li insertion process in Bi_2MoO_6 . The as-synthesized materials are then tested in LIB cells. The results show that the hybrid Bi_2MoO_6 /palm carbon materials give a much improved performance compared to Bi_2MoO_6 .

2. Experimental and Computational Details

2.1. Materials Synthesis

All chemical reagents in our study were analytical grade. The Bi_2MoO_6 material was synthesized by hydrothermal methods. In addition, 2 mmol $\text{Bi}(\text{NO}_3)_3$ and 1 mmol Na_2MoO_4 were dissolved in 20 mL de-ionized water under magnetically stirring for 1 h (h) to form a uniform mixture solution of bismuth molybdate. The mixture solution was then put in a 50 mL hydrothermal reactor and heated by an electric oven at 180 °C for 12 h. The produced precipitates were centrifuged and washed with water and ethanol for several times, and dried under vacuum at 60 °C. Finally, the pure Bi_2MoO_6 was obtained, denoted as BMO.

The palm raw material was first washed with de-ionized water and dried under air at 60 °C. The precursor was then boiled in saturated sodium hydroxide (NaOH) for 6 h at 110 °C and soaked in H_2O_2 (30%) for 12 h at 60 °C. Finally, the obtained precursor was centrifuged and washed with de-ionized water and ethanol, and dried under vacuum at 60 °C. The as-prepared palm was pre-oxidized in a tube furnace at 350 °C for 2 h in oxygen atmosphere. The pre-oxidized sample was then carbonized in a tube furnace at 550 °C for 3 h in argon atmosphere, at a heating rate of 3 °C·min⁻¹.

The as-prepared palm carbon was ultrasonically dispersed in 10 mL de-ionized water for 2 h; the palm carbon solution was then added dropwise to the Bi/Mo mixture, under constant stirring. After one hour of stirring, the mixed solution was transferred into a 50 mL Teflon-lined stainless-steel autoclave and heated in an oven at 180 °C for a duration of 12 h. The obtained precursor was centrifuged and washed with water and ethanol several times, and dried under vacuum at 60 °C. The powders obtained were annealed in a tube furnace with a temperature ramp of 1 °C·min⁻¹ at 550 °C for 2 h, to yield the sample denoted as BMO/C. The weight percentage of palm carbon in the as-synthesized BMO/C sample is 2%, giving a weight ratio of metal oxide to carbon as 49:1.

2.2. Materials Characterization

The crystal structure of the BMO/C was characterized by X-ray diffraction (XRD) using $\text{Cu K}\alpha$ radiation ($\lambda = 0.15406$ nm) under a voltage of 40 KV and a current of 40 mA. Scanning electron microscopy (SEM; JEOL JSM, 6510 V) and scanning transmission electron microscopy (STEM, Hitachi HD2300A, Tokyo, Japan, operated at 200 keV—Schottky field emission gun) are used to characterize the morphology of the prepared compounds. Samples were prepared by dispersing the powder in isopropanol and sonicating them for about 20 min. A drop of solution was filtered through a holey-carbon grid; the grid was dried at 100 °C for 5 min before being transferred to the microscope. Raman spectroscopy of the synthesized powders were conducted using Renishaw 2000 (514 nm green laser, 40 mW) over the range of 100–1000 cm⁻¹. The oxidation states of the samples were investigated using an X-ray photoelectron spectrometer (XPS, Escalab 250Xi, Massachusetts, MA, USA).

2.3. Electrochemical Measurements

The charge and discharge tests were tested by a CR2025 button cell on the battery testing system (Neware, Shengzhen, China). Two working electrodes were prepared, using BMO and BMO/C respectively, as active materials. The working electrodes were made of active material, acetylene black, and Carboxymethylcellulose sodium (CMC) with a molar ratio of 7:2:1. The electrodes were dried at 100 °C in a vacuum furnace for overnight. The separator was Celgard 2400 porous polypropylene. The electrolyte, LiPF₆ (1 mol·L⁻¹), was mixed with ethylene carbonate (EC) and diethyl carbonate (DEC) at a volume ratio of 1:1. Li metal was used as the counter electrode. All the tests were assembled in an argon-filled box containing less than 1 ppm each of oxygen and moisture. The charge and discharge processes were tested at a constant current density of 100 mA/g and a voltage range of 0.01 to 3.00 V. The typical mass of the electrode material used in the experimental ranged from 5 to 8 mg. Electrochemical impedance spectroscopy (EIS) experiments and cyclic voltammetry (CV) were conducted using a CHI 600 E electrochemical workstation.

2.4. Computational Details

Density functional theory (DFT) calculations were conducted in the Vienna Ab initio Simulation Package (VASP, version 5.3.5) [32–35] to elucidate the Li insertion into Bi₂MoO₆. To describe the ion–electron interaction, the projector-augmented wave method (PAW) was used [36]. Based on convergence tests, the plane wave cut-off and k-space integrals were chosen so that the total energy was converged to 1 meV/atom, the kinetic energy cut-offs for all systems were set to 600 eV, with a 6 × 3 × 6 Γ -centered Monkhorst–Pack grid to sample the Brillouin zone [37]. The tetrahedron method with Blöchl corrections for smearing [36–38] was further applied. The generalized gradient approximation (GGA) with Perdew–Burke–Ernzerhof (PBE) [39,40] functionals were used to describe the interacting electron exchange–correlation energy, with an electronic convergence criteria of 10⁻⁵ eV and an ionic convergence criteria of 10⁻³ eV·Å⁻¹. All of the calculations were performed spin-polarized. Bader AIM (Atoms in Molecules) charges [41] were calculated with the Henkelman algorithm [42]. Bi₂MoO₆ is experimentally seen to be a semi-conductor. It is well known that uncorrected GGA underestimates the band gaps of strongly correlated systems due to the DFT electron self-interaction error, and hence we have used the On-site Coulombic interaction (DFT + U) for the Mo *d*-electrons to account for this error [43–46], by means of Dudarev’s approach [47]. Hubbard parameters (U_{eff}) of 8.6 eV for Mo previously parametrized by Getsoian et al. were used [46]. Due to the large polarizability of this Mo upon Li insertion [47–50], the DFT-D3 method with Becke–Jonson damping of Grimme and co-workers [51] was included, as has been successfully applied for this system elsewhere [31].

3. Results and Discussion

3.1. Materials Characterization

Computational Characterization of Bi₂MoO₆

To evaluate energy storage technologies, experimental observations combined with atomistic insights provided by theory (DFT) is an extremely powerful tool. Knowledge of the electronic states, relative occupations, magnetic moments, and oxidation/reduction behavior allows an understanding of the electrochemistry of the system to be elucidated. This is then applied to both the pristine and the defective (here Li interstitials or Li substitutional defects) Bi₂MoO₆ systems, giving atomistic meaning to the experimental Li storage results. Here, firstly, the pristine Bi₂MoO₆ structure before Li addition is studied to understand the atomic scale structure of our anode material, and the effect of Li storage in Bi₂MoO₆ is included in Section 3.4.

Three crystal structures of Bi₂MoO₆ have been investigated: orthorhombic with space group Pca2₁ (Figure 1a), monoclinic P21/c (Figure 1b), and Pbca (Figure 1c). Based on the total energy from cell optimizations of these cells, the orthorhombic Pca2₁ is found to be the most stable structure of

Bi_2MoO_6 , which is in agreement with experiment [26]. It is worth noting that, at higher temperatures, a phase transition from the orthorhombic to monoclinic phase has been observed experimentally [52]. For the application of Bi_2MoO_6 as an anode material for LIBs, the low temperature orthorhombic structure (as shown in Figure 1a) will be used.

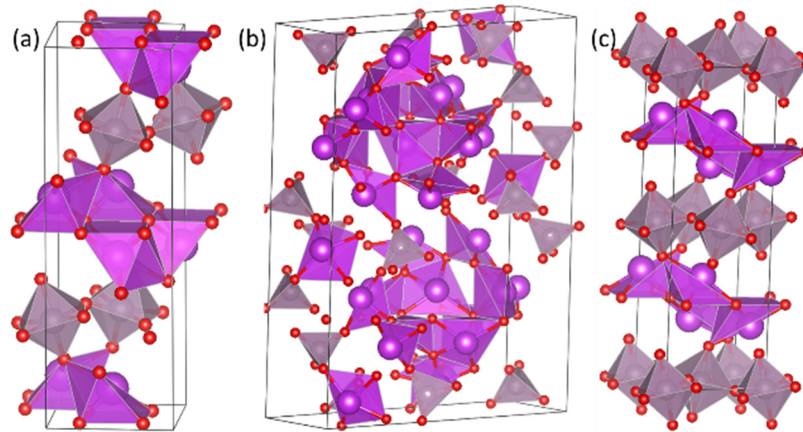


Figure 1. Polyhedral representation of (a) orthorhombic $Pca2_1$, (b) monoclinic $p21/c$, and (c) orthorhombic $Pbca$ structures of Bi_2MoO_6 . Purple spheres are Bi, grey Mo, and red O.

Orthorhombic Bi_2MoO_6 has a layered structure, with alternating layers of corner-sharing MoO_6 octahedra and Bi-O-Bi layers. As discussed in the computational details, non-corrected GGA calculations can result in an underestimation of the electronic band gap. The geometric and electronic structures of orthorhombic Bi_2MoO_6 were optimized with both GGA and GGA + U to understand these differences, as shown in Table 1. It was found that the band gap calculated with GGA underestimated the previously reported experimental band gap by 0.3 eV, whereas including a U-correction gave a band gap of 2.45 eV, which is closer to the measured values of 2.53 eV [53], and 2.56 eV [54], respectively. The GGA + U method also achieved a better agreement with experimental data in terms of lattice parameters, as GGA was found to overestimate the short (a and c) lattice vectors. The obtained lattice parameters with GGA were $a = 5.66 \text{ \AA}$, $b = 16.49 \text{ \AA}$, and $c = 5.68 \text{ \AA}$, with GGA + U giving $a = 5.45 \text{ \AA}$, $b = 16.51 \text{ \AA}$, and $c = 5.47 \text{ \AA}$, as compared to experimental $a = 5.45 \text{ \AA}$, $b = 16.47 \text{ \AA}$, and $c = 5.47 \text{ \AA}$.

Table 1. Comparison of calculated lattice vectors (a , b , and c), angles (α , β , and γ), and band gap.

| | a (Å) | b (Å) | c (Å) | $\alpha = \beta = \gamma$ (°) | E_g (eV) |
|--------------|---------|---------|---------|-------------------------------|----------------------|
| Experimental | 5.45 | 16.47 | 5.47 | 90 | 2.53 [53], 2.56 [54] |
| GGA | 5.658 | 16.491 | 5.676 | 90 | 2.23 |
| GGA + U | 5.448 | 16.506 | 5.467 | 90 | 2.45 |

Calculations of the electronic structure of Bi_2MoO_6 in terms of the projected density of states (PDOS) (Figure 2) reveal that the valence band maximum consists of O p-states, whereas Mo d-states and the Bi p-states make up the conduction band. Utilizing the Bader charge oxidation state convention presented by Getosian et al. [46] for Bi_2MoO_6 , Bader charge analysis confirms the experimental findings of assigning an oxidation number of +3 and +6 for bismuth and molybdenum, respectively. Our calculated Bader charges (per the outlined methodology in Section 2.4) are 1.91 for each bismuth ion, 2.76 for each molybdenum ion, and -1.10 for the oxygen ions, which corresponds to a formal oxygen oxidation state of -2 .

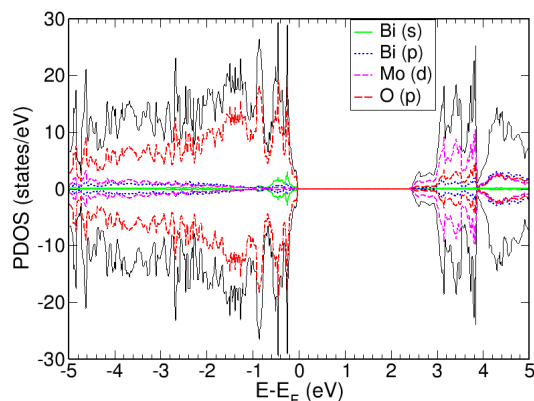


Figure 2. Projected density of states (PDOS) for Bi_2MoO_6 . Energies (E) on the x -axis are referenced to the Fermi level (E_F). All PDOS below $E-E_F = 0$ eV represent occupied states (valence band), whereas those above $E-E_F = 0$ eV, are unoccupied states (conduction band). In addition, positive PDOS values are the α -spin occupations and negative PDOS values are β -spin occupations.

3.2. Experimental Characterization

The crystallographic structures of both BMO and BMO/C samples were examined by X-ray diffraction (XRD). Figure 3a shows all major diffraction peaks appearing at the same lattice planes, at 2θ : 10.927° , 28.309° , 32.533° , 32.642° , 36.055° , 46.737° , 47.175° , 55.585° , 56.251° , and 58.477° , corresponding to the lattice planes (2 0 0), (0 2 0), (1 3 1), (0 0 2), (1 5 1), (2 0 2), (0 6 2), (1 3 3), (1 9 1) and (2 6 2) of the Bi_2MoO_6 structure with high crystallinity (JCPDS card No. 21-0102). These diffraction peaks were furthermore observed in the simulated BMO XRD pattern from DFT calculations (Figure 3b). No other impurity peaks are observed. By comparison, only strong peaks of BMO/C phase were presented in the diffraction peak indexed to the lattice planes (2 0 0) and (0 2 0) corresponding to the lattices planes at 2θ : 10.927° and 32.533° . The difference between the two samples was due to the promoted growth of BMO by palm carbon. In addition, intensity of peaks for BMO/C was so strong that diffraction peaks of carbon was not detected, which is in accordance with the SEM and TEM results. To further investigate the phase of the as-obtained $\text{Bi}_2\text{MoO}_6/\text{C}$, Raman spectroscopy was employed (Figure 3b,c). All the characteristic vibrational bonds for Bi_2MoO_6 can be observed in Figure 3b: 845 cm^{-1} (s), 796 cm^{-1} (vs.), 713 cm^{-1} (m), 402 cm^{-1} (m), 352 cm^{-1} (s), 325 cm^{-1} (w), 292 cm^{-1} (m, sh), 282 cm^{-1} (s), 230 cm^{-1} (w), 195 cm^{-1} (m), 139 cm^{-1} (m) [17]. The band at 139 cm^{-1} originates from the lattice modes of Bi^{3+} atoms mainly in the direction perpendicular to the layers [17,26,48]. The $190\text{--}405\text{ cm}^{-1}$ range mostly corresponds to the stretching and bending modes of BiO_3 tetrahedra, coupled with bending motions of the MoO_6 octahedra [55]; the modes at 282 and 292 cm^{-1} most likely correspond to E_g bending vibration and the ones around 325, 352, and 402 cm^{-1} originate from E_u symmetry bending modes [56]. The less intense peaks in the range of $400\text{--}600\text{ cm}^{-1}$ can be assigned to the stretching modes of the Mo-O bonds and the twisting mode in Bi_2MoO_6 [57]. As for the modes observed above 700 cm^{-1} , the peak at 796 cm^{-1} is attributed to the symmetric stretch of a MoO_6 octahedron, whereas modes at 714 and 844 cm^{-1} represent the orthorhombic distortions of the MoO_6 octahedron in Bi_2MoO_6 [56]. In comparison to BMO, the peaks of BMO/C were found to broaden and slightly shift toward lower wavenumbers [58], in addition to the presence of a small peak at 885 cm^{-1} , originating from the vibration of Mo-O bonds in MoO_4 . Nevertheless, the absence of significant spectral deviation from the samples revealed that the main structure of the Bi_2MoO_6 phase was not dramatically disturbed. To further understand the nature of carbon materials in the BMO/C sample, the sample was examined in the $1000\text{--}2000\text{ cm}^{-1}$ wave number range. Figure 3c shows the Raman spectra of the sample with two peaks appearing at 1353 cm^{-1} (D-band, disordered carbon) and 1589 cm^{-1} (G-band, graphitic carbon). The D-band represents the disordered carbon with defect (i.e., the broken of the 6-member ring symmetry) and the G-band corresponds to the sp^2 hybridized carbon with graphitic carbon (i.e., with the perfect 6-member ring symmetry). The intensity ratio of D-band and G-band (I_D/I_G) gives an

indicator of the degree of disorder of the carbon. Figure 3c shows the intensity ratio of $I_D/I_G = 0.85$, indicating that the sample of BMO/C is present with both graphitic carbon and disordered carbon.

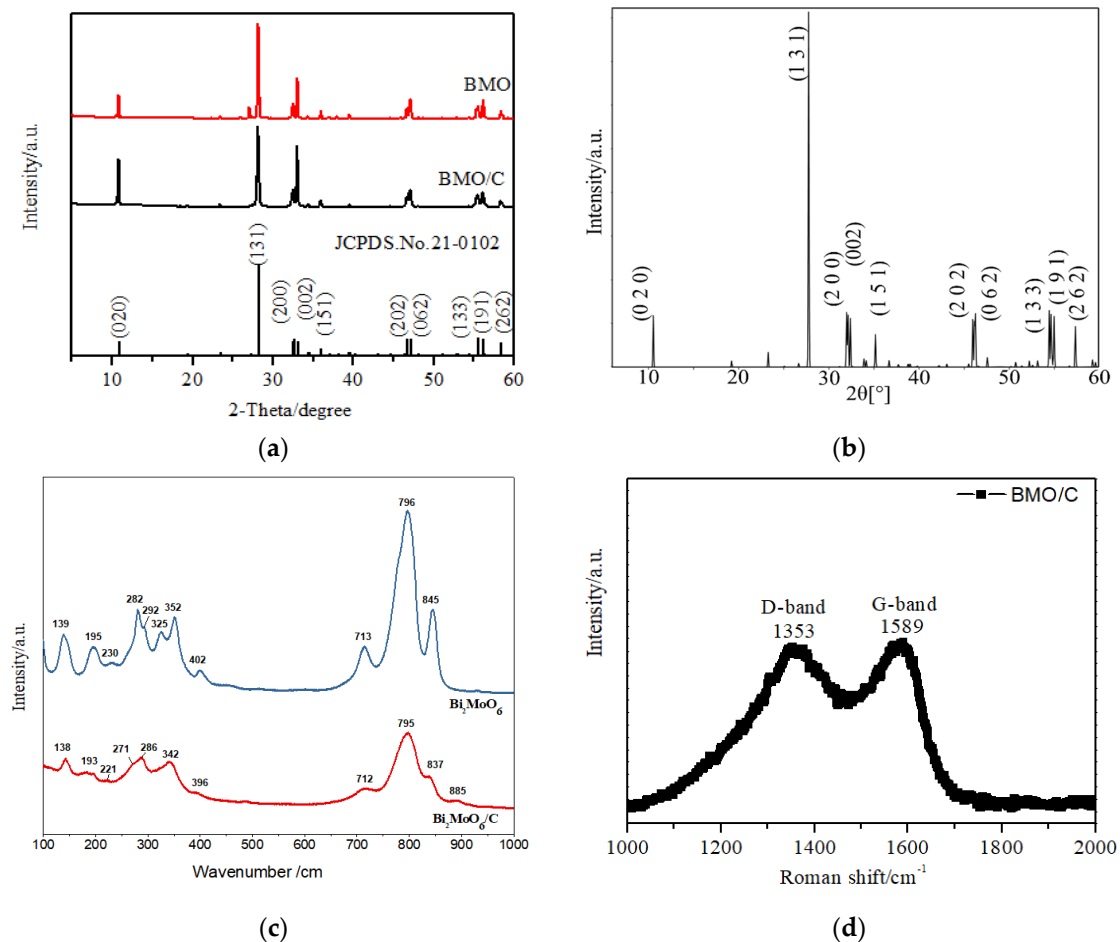


Figure 3. (a) XRD patterns of BMO/C, BMO and standard card, and (b) DFT simulated XRD pattern for BMO (c) Raman spectrum of BMO and BMO/C samples in the wavelength range of $100\text{--}1000\text{ cm}^{-1}$; (d) Raman spectrum of the as-synthesized BMO/C in the wavelength range of $1000\text{--}2000\text{ cm}^{-1}$.

The morphology of the as-synthesized BMO was characterized using SEM and STEM. Figure 4a,c show the SEM images of BMO particles, with a particle length of about $1\text{ }\mu\text{m}$. Figure 4b,d show the SEM images of BMO/C particles of 3D nanosheets, with a particle length of 100 nm . Upon modification with palm carbon, the flakes appear to be shortened and aggregated, becoming more rounded in nature, but of smaller sizes. Figure 4e,f show the STEM images of BMO and BMO/C, respectively. The BMO/C composite image is obtained by overlaying the High-Angle Annular Dark Field image, whose contrast is proportional to the Z^2 of the material, on top of the Secondary Electron image, which reveals the surface morphology of the sample. It also shows that the Bi_2MoO_6 particles are attached to the palm carbon scrolls (green color), confirming the composite nature of the material. This is because the model approximates hydrogenic cross-sections and flat samples, whilst the experimental comparison is between the Bi M-edge and the Mo L-edge; XRD confirms that the crystal structure remains that of the stoichiometric BMO. Figure 4g,h show the statistical analysis of long/short axes ratio for the Bi_2MoO_6 particles in the BMO and BMO/C samples, with an average value around 4.45 for the BMO sample and 1.19 for the BMO/C sample. This indicates that the BMO sample shows three-dimensional slender needles; however, upon modification with palm carbon, the Bi_2MoO_6 particles appear to shorten, becoming more rounded in nature. Figure 4i,j show the statistical analysis of the Bi_2MoO_6 particle size in the BMO and BMO/C samples. It is clear that the particles are much smaller in the BMO/C

sample (with an average particle size of ~482 nm) than those in the BMO sample (with an average particle size of ~154 nm). We conclude that the supply of the palm carbon has a remarkable effect on the morphology of the BMO quasi-nanometer microspheres.

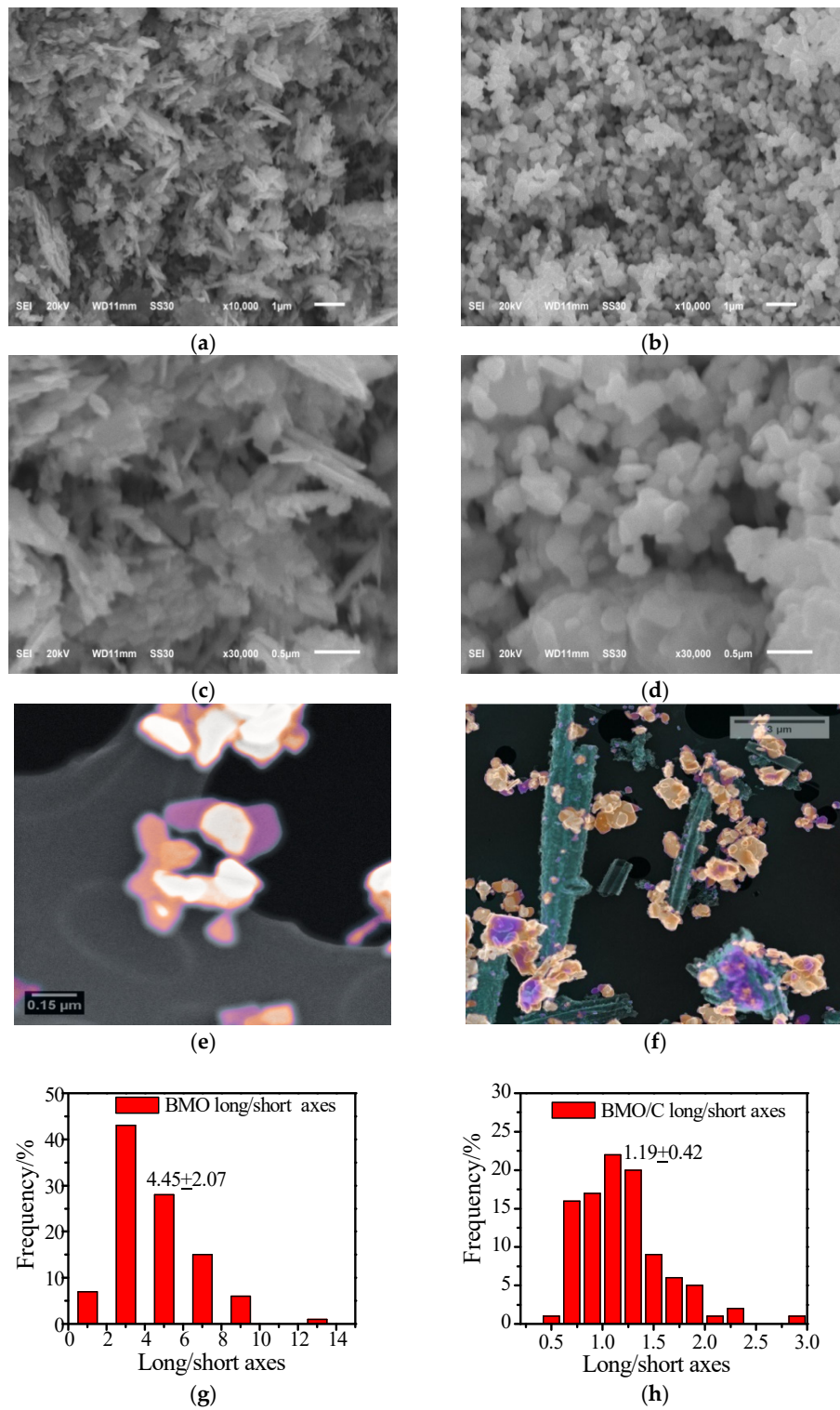


Figure 4. Cont.

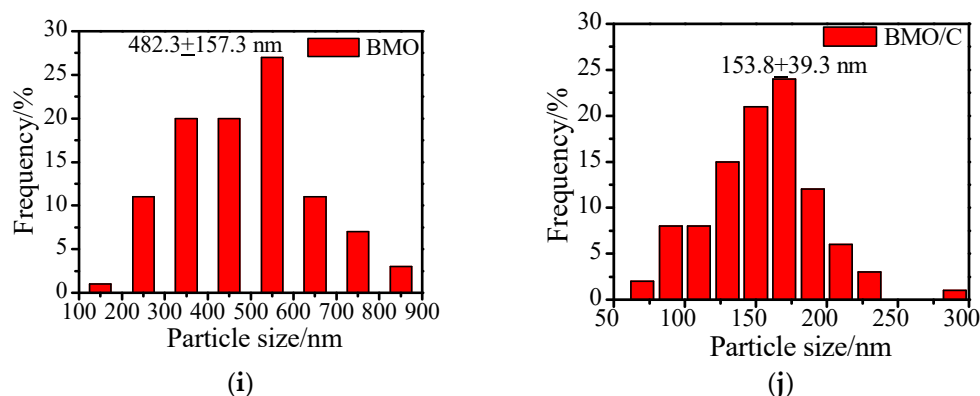


Figure 4. (a,c) low and high magnification SEM images of BMO; (b,d) low and high magnification SEM images of BMO/C; (e,f) composite false-color STEM images of the BMO and BMO/C samples, with the Z-contrast image superimposed on the Secondary electron background image; bright colors signify high Z material (The images have been colorized by assigning the grey scale intensity range to a colour tone range using ImageJ and its look-up-tables Blue-Orange and Thallium for the Z-contrast and the secondary electron image, respectively); (g,h) statistically calculated long/ short axes ratio of the BMO particles in the BMO and BMO/C samples; (i,j) statistically calculated BMO particle size in the BMO and BMO/C samples.

The chemical compositions and the surface electronic states of the BMO/C sample are investigated using XPS, with results shown in Figure 5. All the expected elements including Bi, Mo, C and O can be found in the survey spectra. As shown in Figure 5b, two binding energy peaks appeared at 164.6 eV for Bi 4f_{7/2} and 159.3 eV for Bi 4f_{5/2}, revealing that Bi is in the Bi³⁺ oxidation state. Figure 5c shows two peaks with binding energies of 235.8 and 234.2 eV which are assigned to the Mo⁶⁺ ions, respectively. The peak of the O 1s spectrum was observed at 530.27 eV, which is attributed to the lattice oxygen and near surface oxygen in bismuth molybdate [25,26]. The analysis of XPS shows two obvious peaks at 284.5 eV and 286.2 eV, corresponding to C-C sp², and C-C sp³, respectively. A slight O=C=O peak at 288.6 eV is observed, due to the pre-oxidation of the sample [26]. The XPS results confirm the composition of the BMO/C sample as inferred from EDX and XRD and show that the surface is oxygen deficient, which is expected to help improve the performance.

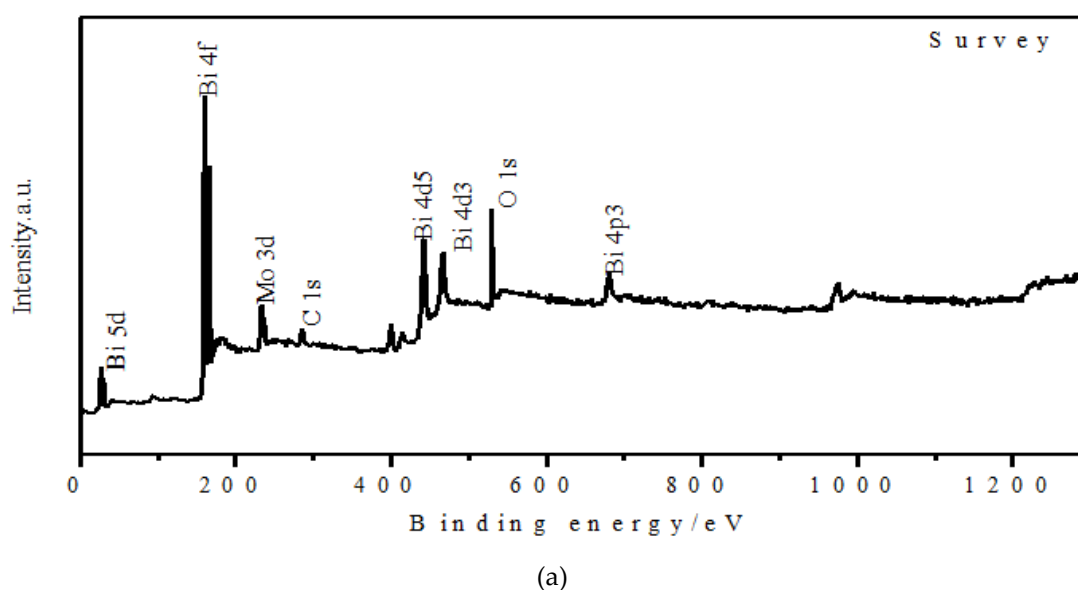


Figure 5. Cont.

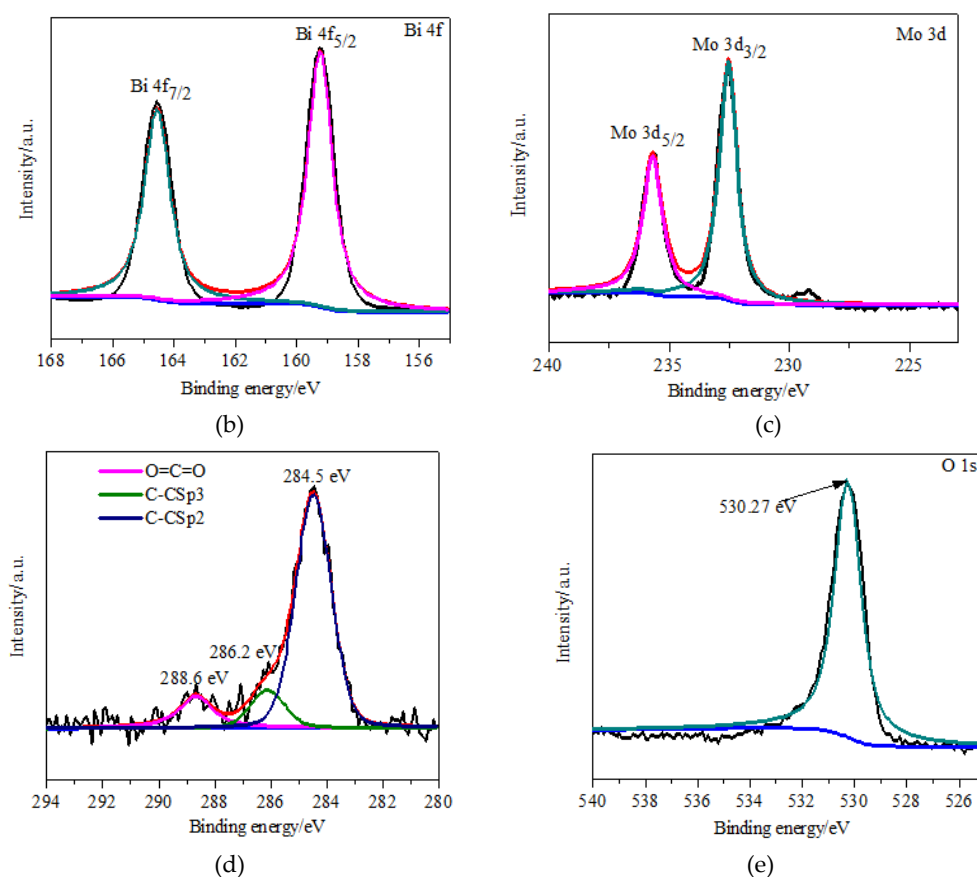


Figure 5. XPS spectra of the BMO/C sample: (a) survey, (b) Bi 4f, (c) Mo 3d, (d) C 1s, (e) O 1s.

3.3. Electrochemical Properties

Figure 6a,b show the discharge and charge curves of BMO and BMO/C electrodes during 1st, 2nd and 20th cycles at a constant current density of $100 \text{ mA}\cdot\text{g}^{-1}$ and a voltage range of 0.01 to 3.0 V (vs. Li^+/Li). It can be seen from Figure 6a that BMO features two plateaus at approximately 0.65 V and 0.75 V; the initial discharge and charge specific capacity of the BMO electrode are 841 and $753 \text{ mAh}\cdot\text{g}^{-1}$, with an initial columbic efficiency of 89% (which is the ratio of the first cycle discharge capacity to the first cycle charge). From Figure 6a, we can infer that the reaction during the first discharge involves intercalation of Li into the BMO lattice, followed by the destruction of the crystal structure, the amorphization of the BMO lattice, and finally the formation of Bi and Mo metals [20]. Figure 6b shows that BMO/C also features two plateaus at about 0.5 and 0.6 V which are less than the plateaus of BMO, and the initial discharge and charge specific capacity of the BMO/C electrode are 1014 and $889 \text{ mAh}\cdot\text{g}^{-1}$, with an initial columbic efficiency of 87%. The enhanced performance of BMO/C can be attributed to two factors: (1) the more rounded shape of the BMO particles, providing more reacting surface sites [59–62]; (2) palm carbon materials that improve the ionic and electronic transport and make more BMO reaction sites accessible hence increase the storage capacity.

Figure 6c shows the cycling performance and the columbic efficiency of the BMO and the BMO/C electrodes. The cycling performance of the BMO/C electrode is superior to the BMO electrode. The specific capacities of both electrodes decrease after 20 cycles, with the BMO/C electrode maintaining a capacity of $731 \text{ mAh}\cdot\text{g}^{-1}$ and the BMO electrode retaining a capacity of $580 \text{ mAh}\cdot\text{g}^{-1}$. At a current density of 100 mA/g , the loss of the second cycle discharge specific capacity of BMO/C is 8% less than that of BMO. Remarkably, the increase of the capacity is attributable to the fragmentation of BMO/C particles during the cycling process, which increases the contact of the material with the electrolyte and thus the specific capacity. This is similar to the behavior of transition metal oxide anodes such as Co_3O_4 [60,61] and ZnMn_2O_4 [62]. The BMO/C electrode achieved a high reversible capacity of 664

$\text{mAh}\cdot\text{g}^{-1}$ after 200 cycles, while the BMO electrode only obtained a capacity of $282 \text{ mAh}\cdot\text{g}^{-1}$ after 200 cycles. The BMO/C electrode in this work shows improved cycle performance compared to the reported $\text{Bi}_2\text{MoO}_6/\text{reduced graphene oxide}$ composites, which has a retention capacity of $705 \text{ mAh}\cdot\text{g}^{-1}$ after 100 cycles [26]. Figure 6d shows the capacity retention at load current densities of 100, 200, 500 and $1000 \text{ mA}\cdot\text{g}^{-1}$; the discharge specific capacities of the BMO/C electrode are $501, 426, 380$ and $332 \text{ mAh}\cdot\text{g}^{-1}$. The specific capacity could be recovered to $547 \text{ mAh}\cdot\text{g}^{-1}$ when the load current density is returned to $100 \text{ mA}\cdot\text{g}^{-1}$. The BMO electrode, however, gives a much lower specific capacity under the same condition. The specific capacities of the BMO electrode measured at the same current densities are $436, 361, 320$ and $283 \text{ mAh}\cdot\text{g}^{-1}$. With the current density being brought back to $100 \text{ mA}\cdot\text{g}^{-1}$, the retained capacity is $484 \text{ mAh}\cdot\text{g}^{-1}$. The better electrochemical properties of BMO/C could be ascribed to the presence of palm carbon [63,64], which facilitates the charge transfer process in the BMO/C layers. In addition, the fragmentation of the BMO structure during cycling [17–19] provides a higher number of smaller BMO particles, and thus higher surface area and access for electrochemical reactions with Li. The reactions of Li with ternary oxides such as Bi_2MoO_6 involve multistep reactions which include: intercalation, conversion reactions (i.e., Bi and Mo are electrochemically active with respect to Li) and alloying under further reduction of Bi^{3+} to Bi. Extra discharge capacity can be obtained from the formation of Li–Bi alloy [17–19]. These factors lead to a significant improvement of the electrochemical performance for Li-ion batteries [16,18,26].

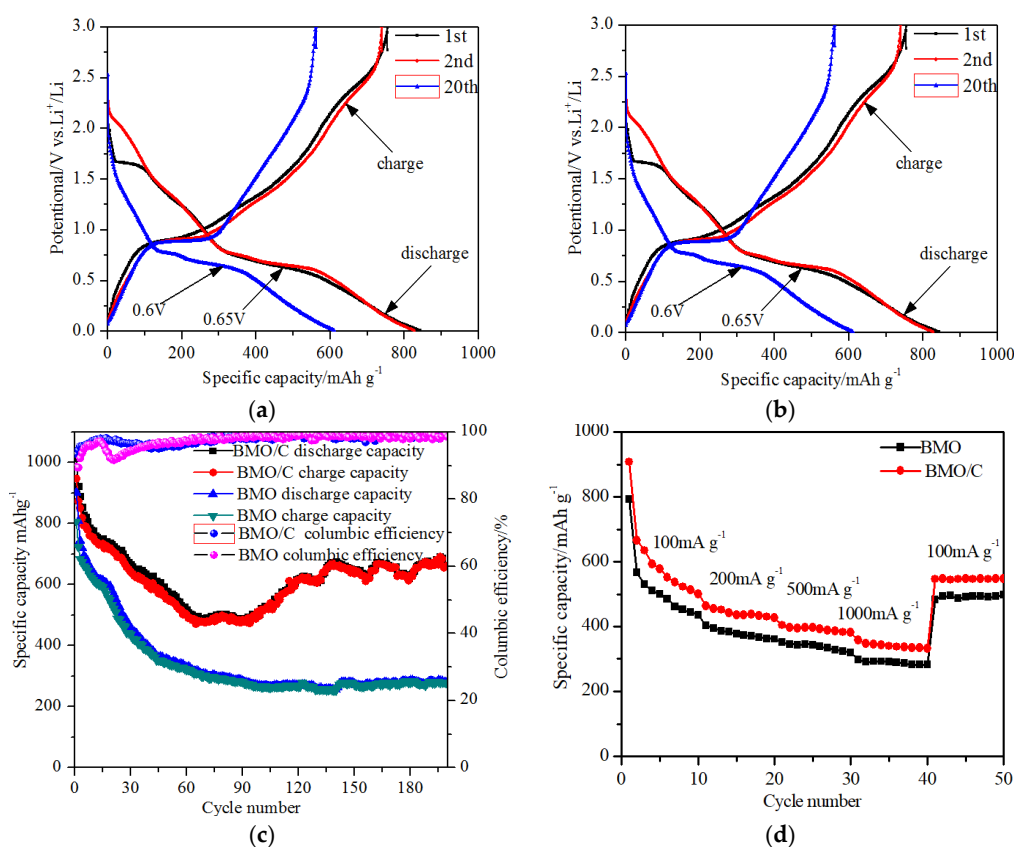


Figure 6. Discharge and charge curves of (a) BMO, (b) BMO/C electrodes for the 1st, 2nd and 20th cycle at a constant current density $100 \text{ mA}\cdot\text{g}^{-1}$, and (c) cycling performance and the corresponding columbic efficiency of BMO and BMO/C electrodes at current density of $100 \text{ mA}\cdot\text{g}^{-1}$, (d) discharge and charge rate performance of BMO and BMO/C electrodes at current densities of 100, 200, 500, 1000 and $100 \text{ mA}\cdot\text{g}^{-1}$.

Figure 7a shows the electrochemical impedance spectra (EIS) of the samples acquired in the frequency range of 0.01 and 100 KHz. The EIS measurement was carried out with fresh cells at an

open circuit voltage (OCV) of 2.21 eV and 2.60 eV, respectively, for the BMO and BMO/C electrodes. The intercept of the semicircle appearance of the high frequency is attributed to the ohmic resistance (the electrolyte resistance, R_s) [65] in the equivalent circuit, which is related to the solid electrolyte interphase (SEI) film and the contact resistance. The semicircle in the medium frequency region corresponds to the charge transfer between the electrode and electrolyte. The semicircle is interpreted as a parallel circuit which consists of the double layer capacitance [66], C_{dl} , and the charge transfer resistance [67], R_{ct} . The inclined lines in the low frequency range are related to the lithium ion diffusion in the BMO and BMO/C electrodes, and are associated with Warburg impedance [68,69] Z_w in the equivalent circuit. The resistance of BMO/C electrode of 138 Ω is lower than that of the BMO electrode (with a resistance of 246 Ω). The result indicates that the BMO/C electrode exhibits better electronic conductivity than the BMO electrode. Das et al. reported the electrochemical impedance spectroscopy (EIS) and the Nyquist (Z' Vs. $-Z''$) plots of a Li/Co₂Mo₃O₈ system at a current density of 60 mA/g and a voltage range of 0.05–3 V during the first discharge and charge cycle [23]. When the OCV is 2.7 V, the Nyquist plot showed a semicircle in the high frequency range and an arc type in the low frequency range. It was indicated that, when the OCV decreases to 1.5 V, the Nyquist plot had no significant change except a decrease in the overall impedance. When the discharged voltage was close to 0.005 V, the second semicircle appeared in the intermediate frequency region at 0.9 V, which was attributed to the impedance from the bulk. This was consistent with the galvanostatic cycling data, which indicated the destruction of the crystal structure [23]. The impedance values during the first discharge/charge cycle supported the reaction mechanism which had the crystal structure destruction and reaction, as reflected by an increase in the overall impedance value until 0.005 V. When charged, the overall impedance value decreased with the reformation of corresponding metal oxides [20–23].

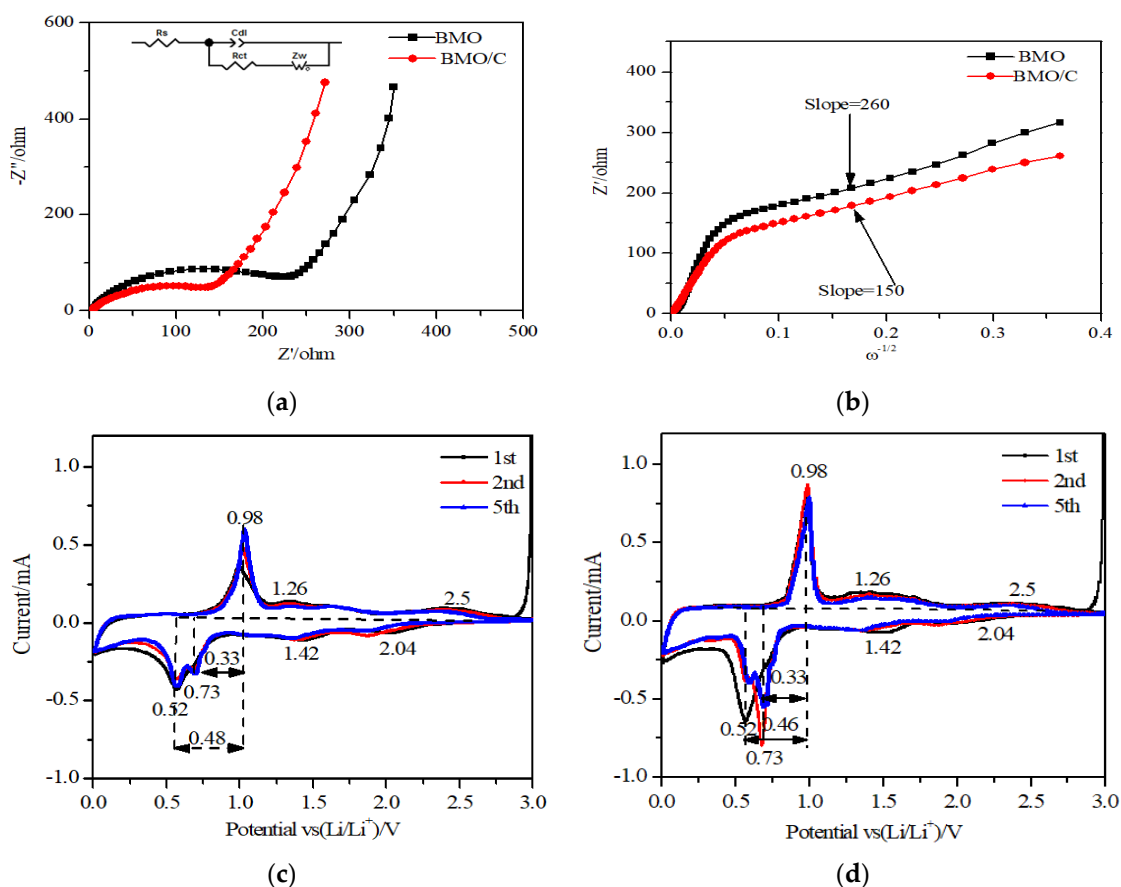


Figure 7. (a) electrochemical impedance spectra (EIS) of the BMO and BMO/C; (b) linear fitting of Warburg impedance of the BMO and BMO/C electrodes; cyclic voltammograms and FWHM for the 1st, 2nd and 5th cycles of (c) BMO and (d) BMO/C electrodes at the rate of 0.1 mVs⁻¹.

Figure 7b shows the linear fitting Warburg impedance of BMO and BMO/C. The Warburg impedance represents the impedance that is generated by the diffusion of Li ions [70] in the lattice of electrode material. According to the formula $Z' = R_s + R_{ct} + A_w \omega^{-1/2}$, A_w is related to the slope of the Warburg impedance diagram, and ω is assigned to the angular frequency of the alternating current. The Li^+ diffusion coefficient in the electrode can be estimated using Equation (1):

$$D_{\text{Li}^+} = 0.5 \left[\frac{V_m}{FSA_w} \left(-\frac{dE}{dx} \right) \right]^2 \quad (1)$$

where V_m is the molar volume of the material, F is the Faraday constant, S is the apparent surface area of the electrode, and $(dE)/(dx)$ is the slope of the open circuit potential vs. the mobile ion concentration x at each x value. Based on the molar volume, the electrode surface area and $(dE)/(dx)$ were substantially the same. The Li ion diffusion coefficient is proportional to the Warburg coefficient $(1/A_w)^2$. The Warburg coefficient (A_w) of BMO and BMO/C are 260 and 150 $\Omega\text{s}^{-1/2}$, which confirms that the ionic conductivity of BMO/C is better than that of BMO.

We also evaluated the electrochemical performance using cyclic voltammograms (CVs). Figure 7c,d show CV curves of the BMO electrode and the BMO/C electrode for the 1st, 2nd and 5th scan, at a scan rate of 0.01 mVs^{-1} in the potential range of 0.01 to 3.0 V vs. Li/Li^+ . It is worth noting that the scan rate is low enough to obtain accurate estimation of the diffusion coefficient. The FWHM of each peak are marked in Figure 7c for BMO and Figure 7d for BMO/C. The FWHM of BMO for the 1st cycle is 0.48 V, while the FWHM of BMO/C is 0.52 V. In addition, after the first oxidation and reduction, the reduction peaks shifted to 0.73 V, indicating the formation of irreversible phase and the reduction of irreversible electrolytes [22]. Normally, the irreversible capacity loss (ICL) is related to the intrinsic properties of metal oxides, the decomposition of electrolyte accompanied by the SEI formation [22]. The FWHM of BMO and BMO/C for the 2nd and 5th are 0.33 V, which corresponded to the stable reversibility of the BMO and BMO/C during the lithium-ion intercalation and deintercalation process. The cathodic peak which appeared at 2.04 V during the first negative scan could be assigned to the formation of $\text{Li}_x\text{Bi}_2\text{MoO}_6$, as a result of lithium ions inserted into the layered structure of Bi_2MoO_6 crystal. The small peak at 1.42 V is related to the reduction of Bi_2MoO_6 to Bi and Mo metal [29,31]. During the first cathodic scan, two reduction peaks appeared at 0.52 V and 0.73 V. The obvious cathodic peak at 0.52 V can be associated with the alloying reaction of Bi and Li to form Li_3Bi [29,31]. Furthermore, the other broad reduction peak is located at 0.73 V, which is related to the two-step formation of LiBi and Li_3Bi in the electrochemical lithiation reaction process. A strong oxidation peak is observed at 0.98 V, which could be associated with the de-alloying process of Li_3Bi to Bi [29,31]. Two small anodic peaks appeared at about 1.26 and 2.50 V during charging, which can be attributed to the formation of lithium molybdate and Li_2O [29,31]. Figure 7d shows the CVs of BMO/C electrode under the same conditions. The results suggest that the anodic peaks of the BMO/C electrode at around 0.52 V in the first sweep move to higher voltages, which could be assigned to the smaller polarization of the BMO/C electrode compared to the BMO electrode. It is worth noting that the peaks of the BMO/C electrode are sharper relative to BMO, and the area between the oxidation peak and the reduction peak is narrower. This indicates that the transfer resistance of Li^+ in the BMO/C composite is smaller and the rate of redox is higher. Furthermore, the more rounded particle shape of BMO/C is associated with a shorter diffusion length, thus the polarization of BMO/C is weaker than that of BMO. After the first cycle, the reduction and oxidation peaks in the CV curves overlap. This indicates that the electrode shows good reversibility and stability over cycling. The above analysis gives us the basis to postulate the electrochemical reaction mechanism of the BMO electrodes as follows (reactions (1)–(4)).





3.4. Modelling of Li Insertion in the Bi_2MoO_6 Lattice

Atomic scale simulations provide a means to evaluate local structure and help to understand the factors influencing the electrochemical behavior of battery materials. Computational techniques have been proven to be very useful for understanding Li incorporation in other oxides previously [70–72]. Hence, we have used DFT simulations to model the Li insertion in Bi_2MoO_6 , to give insights into the local structure properties at the atomic scale. The Bi and Mo layers within the Bi_2MoO_6 lattice are strongly bonded, and hence the breaking of this bonding is unlikely to occur [31]. Firstly, substitutional Li defects were investigated by replacing the cations with one Li. The defect formation energy (E_f) [73] of this substitutional defect (Li_A) ($A = \text{Bi}, \text{Mo}$) was calculated according to

$$E_f(\text{Li}_A) = E_{\text{Li}_A} - E_{\text{bulk}} + \mu_A - \mu_{\text{Li}} \quad (2)$$

where E_{Li_A} is the total energy of the system with Li on A site, E_{bulk} is the total energy of the system without the defect, μ_A is the chemical potential of A, and μ_{Li} the chemical potential of Li. The chemical potentials have been taken as the total energy for a single metal atom from Bi, Mo, and Li metallic bulks, respectively. To evaluate the different inequivalent Bi and Mo lattice sites for Li substitution, the Site-Occupancy Disorder program (SOD) [74] was employed. These inequivalent substitutional lattice sites are shown graphically in Figure 8a–c, respectively. Two inequivalent lattice sites for Bi_{Li} were found, whereas all Mo_{Li} were equivalent.

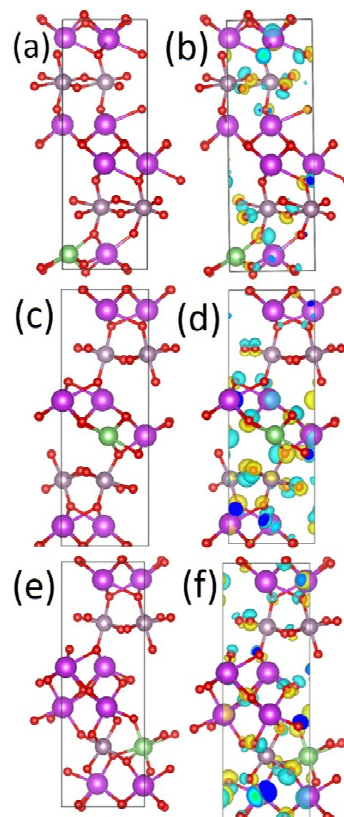


Figure 8. Side view of the optimised Li substitutional defects for (a) Li_{Bi} site one, with charge density difference plot in (b), (c) Li_{Bi} site two, with its corresponding charge density plot in (d), and (e) Li_{Mo} and its charge density difference plotted in (f). Purple spheres are Bi, grey Mo, green Li, and red O. Yellow iso-surface represents an increase in charge density upon lithium substitution, whereas blue represents depletion of charge density.

Calculating the defect formation energy of Li substitutional defects according to Equation (2), the formation energy for Li substitution on Bi site (Li_{Bi}) is 2.31 eV, and 2.35 eV, on site one and two respectively (Figure 8), with the Li on a Mo site (Li_{Mo}) giving a much higher defect formation energy of 8.15 eV. It is hence seen that Li substitution of Bi is more energetically favorable than Mo-substitution. Examining the differences in charge density induced by Li substitution (Figure 8), it is seen that both Mo_{Li} and Bi_{Li} cause wide disruption to the charge distribution, with the extra charge density mainly located on the oxygen lattice. Hence, Li substitutional defects could induce the formation of local electric fields, improving the battery performance, but, as these defects have high formation energies, Li substitutional defects are not energetically favorable in the Bi_2MoO_6 lattice. Next, Li on interstitial lattice sites is simulated. Interstitial lithium ions in other oxide-based battery materials have previously been postulated by computational and experimental studies [70,72].

For Li interstitial lattice sites, equivalent lithium lattice positions have to be considered. The defect formation energy [73] of Li interstitial in Bi_2MoO_6 (Li_{int}) was calculated from Equation (3):

$$E_f(Li_{int}) = E_{Li_{int}} - E_{bulk} - n\mu_{Li} \quad (3)$$

Here, $E_{Li_{int}}$ is the total energy of the system with the Li interstitial, E_{bulk} is the total energy of Bi_2MoO_6 without impurities, n is the number of Li atoms in the structure, and μ_{Li} is the chemical potential of Li as described above. The defect formation energy of a single Li at different interstitial sites in the Bi_2MoO_6 lattice is presented in Table 2.

Table 2. Defect formation energy (E_f) in eV, average Bader charges (q) with standard deviation, and unique Bader charge for nearest neighbor (NN) atoms to Li site (in e) for insertion of a single Li at different lattice sites. Graphical representation of interstitial site numbering is presented in Figure 9. For comparison, $q_{Bi} = 1.91$ e, $q_{Mo} = 2.76$ e, and $q_O = -1.10$ e for pristine Bi_2MoO_6 .

| Site | E_f | q_{Bi} | $q_{Bi,NN}$ | q_{Mo} | $q_{Mo,NN}$ | q_O | $q_{O,NN}$ | q_{Li} |
|------------------------------|-------|-----------------|-------------|-----------------|-------------|------------------|---------------------|----------|
| BiO-layer | | | | | | | | |
| 1 | -1.79 | 1.85 ± 0.03 | 1.83, 1.85 | 2.68 ± 0.08 | 2.55, 2.67 | -1.08 ± 0.05 | -1.05, -1.11, -1.10 | 0.51 |
| 2 | -1.44 | 1.83 ± 0.02 | 1.79 | 2.64 ± 0.03 | 2.60, 2.67 | -1.07 ± 0.05 | -1.03, -1.08, -1.15 | 0.52 |
| 3 | -1.79 | 1.85 ± 0.03 | 1.80, 1.82 | 2.70 ± 0.08 | 2.57, 2.73 | -1.09 ± 0.04 | -1.12, -1.07, -1.11 | 0.62 |
| MoO₆-layer | | | | | | | | |
| 4 | -2.34 | 1.87 ± 0.02 | 1.89, 1.85 | 2.75 ± 0.06 | 2.66, 2.82 | -1.11 ± 0.04 | -1.08, -1.15 | 0.63 |
| 5 | -2.45 | 1.88 ± 0.02 | 1.87 | 2.72 ± 0.07 | 2.62, 2.80 | -1.10 ± 0.04 | -1.04, -1.09 | 0.61 |
| In-between layers | | | | | | | | |
| 6 | -1.45 | 1.84 ± 0.02 | 1.81, 1.82 | 2.61 ± 0.09 | 2.70, 2.46 | -1.07 ± 0.05 | -1.09, -1.10 | 0.54 |

As opposed to Li substitutional defects, the Li defect formation energy is negative, indicating that Li interstitials are energetically favorable to be present in this system. Li interstitial sites are present in both the MoO_6 -layer and the BiO-layer. Comparing $E_f(Li_{int})$, the introduction of a single Li interstitial at different lattice sites, it is seen that Li interstitials in the MoO_6 -layer are more energetically favorable than a Li interstitial in the BiO-layer. Examining the difference in lattice response to Li interstitial in terms of charge density (Figure 9), it is clear that Li interstitials in the BiO-layer lead to a larger charge density difference than the equivalent process for a Li interstitial in the MoO_6 -layer. This more concentrated redistribution of charge for the Li interstitial in MoO_6 -layers could be favorable for electrochemical performance, forming a local electric field around the Li interstitial.

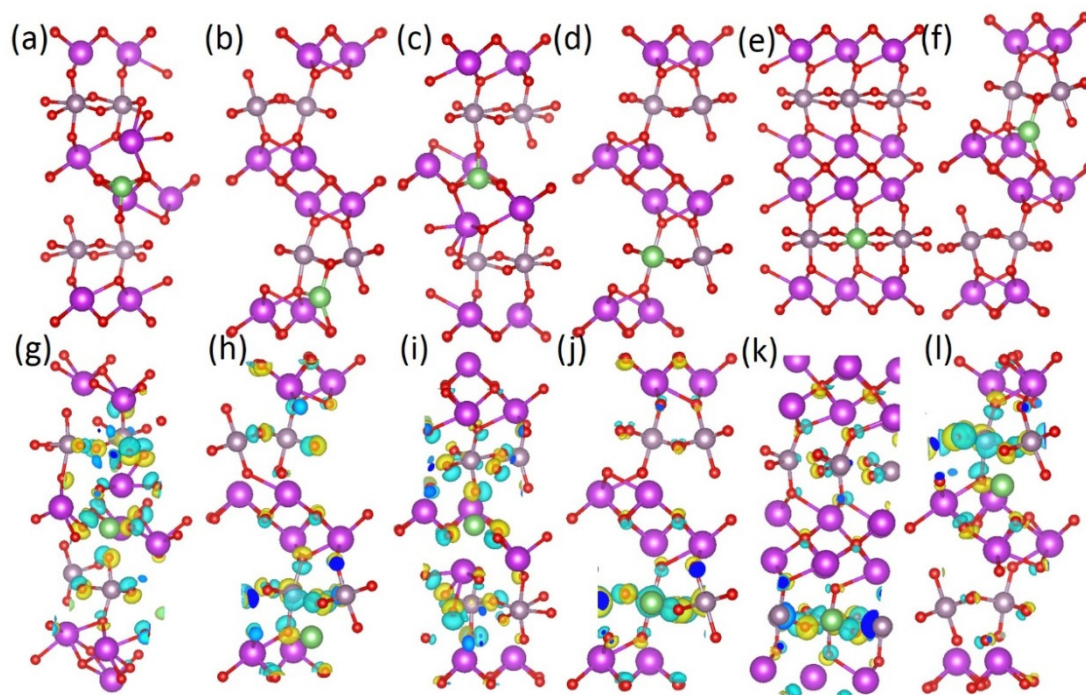


Figure 9. Calculated atomic scale models of Li interstitial in Bi_2MoO_6 at (a) site 1, (b) site 2, (c) site 3, (d) site 4, (e) site 5, and (f) site 6, and charge density difference as a result of Li interstitial at (g) site 1, (h) site 2, (i) site 3, (j) site 4, (k) site 5, and (l) site 6 in Bi_2MoO_6 . The site numbering refers to Table 2. Purple spheres are Bi, grey Mo, green Li, and red O. Yellow iso-surface represents an increase in charge density upon lithium substitution, whereas blue iso-surface represents depletion of charge density.

Examining the change in average Bader charges (Table 2) from the pristine Bi_2MoO_6 cell to the system with Li interstitials, it is seen that the average Bi, Mo, and O charges remain close to their Bi_2MoO_6 values. Examining the change in Bader charge to the species nearest to the Li interstitial site (Table 2), it is observed that upon introducing a Li interstitial in the Bi layer, or in between the layers, the nearest Bi ions to the Li are reduced, as compared to the bulk, by ~ 0.1 e. Li interstitials in the molybdenum layer do not show any such clear change in the Bi charge state. Finally, in all systems, the standard deviation between the Bi Bader charges is less than 0.03 e, indicating on average no change in the Bi oxidation state. Similar observations are made for the oxygen charges, where a wider charge distribution upon the inclusion of a Li interstitial is seen, centered around the pristine Bi_2MoO_6 value. However, it is important to note that slight (< 0.1 e) reductions and increases of charge near the lithium interstitial sites occur on the oxygen ions. For Mo, the introduction of Li interstitials to the system does reduce the neighboring Mo ions Bader charge markedly by between 0.05 to 0.2 e. This could indicate a change from Mo^{6+} to Mo^{5+} , or a mixed 5+/6+ charge state. Li interstitials in the molybdenum layer also increase the molybdenum Bader charge, by a maximum of 0.06 e, as compared to the pristine bulk. This does not, however, indicate a change to a higher oxidation state [46].

Finally, previous computational studies have shown that the DFT-derived defect formation energies can be used to calculate cell voltage trends [75–81]. The cell voltage vs. Li/Li^+ (V) was calculated using the following formula [76,78,79,82]:

$$V = \frac{-E_f(\text{Li}_{int})}{nz} \quad (4)$$

where n is the number of lithium interstitial, and z is the formal charge of Li. Hence, the cell voltage vs. Li/Li^+ for the system calculated here for the most favourable Li interstitial site is 2.45 eV. Furthermore, this and all calculated cell voltages sit within the experimental range.

Following the identification of the MoO_6 -layer as the most favorable layer for Li interstitial sites, the concentration of Li interstitials per molybdenum (x) in the lattice was investigated, up to a total of 1:1 of Li: Mo ratio ($x = 1.00$). Higher Li: Mo ratios were found to lead to heavy distortions of the Bi_2MoO_6 lattice and are hence not presented here. The formation energy $E_f(\text{Li}_{int})$ and Li incorporation energy per Li interstitial ($E_f(\text{Li}_{int})/n$) are presented in Table 3.

Table 3. Formation energy of a Li interstitial defect, and Li incorporation energy for different numbers of Li (n_{Li}) in lattice.

| n_{Li} | $E_f(\text{Li}_{int})$ (eV) | E_{incorp} (eV/Li) |
|-----------------|-----------------------------|----------------------|
| 1 | −2.45 | −2.45 |
| 2 | −4.38 | −2.19 |
| 3 | −6.58 | −2.19 |
| 4 | −7.79 | −1.95 |

From Table 3, it can be seen that the formation of interstitial Li defects is energetically favorable at all x investigated here; the incorporation of Li interstitials in the Bi_2MoO_6 lattice is also favourable, in terms of the incorporation energy ($E_f(\text{Li}_{int})/n$) per Li atom. However, it is worth noting that $E_f(\text{Li}_{int})/n$ decreases with increasing x . When examining the electronic structure of $\text{Li}_x\text{Bi}_2\text{MoO}_6$, it is found that the defect states induced by the Li interstitials are introduced in the band gap. This changes the character of the valence band and conduction band maxima, and thus the Li ion incorporation energy. Nevertheless, the semi-conductor properties of Bi_2MoO_6 are maintained.

4. Conclusions

In this work, Bi_2MoO_6 /carbon (in brief, BMO/C) composite materials have been successfully synthesized by hydrothermal route. XRD and DFT simulations demonstrated that Bi_2MoO_6 in the BMO/C composite has the orthorhombic structure. The relative peak intensities of BMO/C are higher than BMO, indicating that the crystallinity of Bi_2MoO_6 in the BMO/C composite is increased over that of pure Bi_2MoO_6 . SEM show Bi_2MoO_6 rectangle flakes with the size of $\sim 1 \mu\text{m}$, whilst the BMO/C composite showed more rounded and smaller ($0.2 \mu\text{m}$), faceted Bi_2MoO_6 flakes, connected with the carbonized palm. The chemical compositions and surface electronic states of the manufactured products were investigated by XPS, confirming the chemical compositions of the materials as expected. The electrochemical performances of Bi_2MoO_6 and its composite BMO/C were tested when used as an anode material for Li ion batteries. The initial discharge specific capacity of the BMO/C electrode was $1014 \text{ mAh}\cdot\text{g}^{-1}$ and remains at $664 \text{ mAh}\cdot\text{g}^{-1}$ after 200 cycles, much higher than that of Bi_2MoO_6 . It is worth noting that this good performance of the BMO/C electrode is achieved based on a simple synthesis process and using sustainable low-cost palm carbon, which makes it suitable for large-scale practical applications.

The Li incorporation mechanism was also estimated by CV for both Bi_2MoO_6 and its composite BMO/C. The results indicated that the two materials have the same charge and discharge mechanism. Furthermore, the EIS results show that the BMO/C have lower surface layer resistance, which can improve the electronic conductivity and the electrochemical activity. DFT studies show the fundamental mechanisms of Li ion incorporation into Bi_2MoO_6 as Li insertion via the interstitial sites into the MoO_6 -layer. These studies confirm that the improved electrochemical performance of the BMO/C composite is mainly attributed to the enhanced electronic conductivity and more Bi_2MoO_6 reaction sites made accessible by palm carbon. All the results show that the BMO/C composite will promote a novel anode material application for Li ion battery.

Author Contributions: T.Z. synthesized the BMO and BMO/palm carbon samples, carried out the XRD, SEM, and XPS measurement of the samples, and conducted the electrochemical testing for the Li-ion battery cells. E.O. conducted the DFT simulations and analysis. M.C. did the Raman Spectra analysis. V.S. did the TEM measurement and analysis. T.Z. and E.O. drafted the article, revised and edited the manuscript. M.C. and V.S.

contributed to the writing of the Raman and TEM results. C.F., H.W., S.W., and Q.C. provided supervision and funding. C.F. and Q.C. coordinated the collaboration and the necessary work. Q.C. revised and edited the final manuscript and did correspondence with the journal. All authors have read and agreed to the published version of the manuscript.

Funding: This research was funded by the Engineering and Physical Sciences Research Council (EPSRC) grant number EP/M027066/1 and EP/R021554/2, and the Natural Science Foundation of China grant number 21476063.

Acknowledgments: Financial support by the Natural Science Foundation of China (No. 21476063) is gratefully acknowledged. E.O. and Q.C. would like to acknowledge the financial support from the Engineering and Physical Sciences Research Council (EPSRC) in the UK (Grant No. EP/M027066/1; EP/R021554/2), and the use of Athena at HPC Midlands+, which was funded by the EPSRC (Grant No. EP/P020232/1), in this research, and the Eureka HPC cluster at the University of Surrey. V.S. acknowledges support from EPSRC (Grant No. EP/N006372/1).

Conflicts of Interest: The authors declare no conflict of interest.

References

1. Hawley, W.B.; Li, J. Electrode manufacturing for lithium-ion batteries—Analysis of current and next generation processing. *J. Energy Storage* **2019**, *25*, 100862. [[CrossRef](#)]
2. Gauthier, M.; Carney, T.J.; Grimaud, A.; Giordano, L.; Pour, N.; Chang, H.H.; David, P.F.; Simon, F.L.; Odysseas, P.; Christoph, B.; et al. The electrode-electrolyte interface in li-ion batteries: Current understanding and new insights. *J. Phys. Chem. Lett.* **2015**, *6*, 4653–4672. [[CrossRef](#)] [[PubMed](#)]
3. Nishi, Y. Lithium ion secondary batteries; past 10 years and the future. *J. Power Sources* **2001**, *100*, 101–106. [[CrossRef](#)]
4. Giubileo, F.; Bartolomeo, A.D. The role of contact resistance in graphene field-effect devices. *Prog. Surf. Sci.* **2017**, *92*, 143–175. [[CrossRef](#)]
5. Huiqiao, L.; Haoshen, Z. Enhancing the performances of Li-ion batteries by carbon-coating; present and future. *Chem. Commun.* **2012**, *48*, 1201–1217.
6. Kang, X. Electrolytes and Interphases in Li-Ion Batteries and Beyond. *Chem. Rev.* **2014**, *114*, 11503–11618.
7. Kang, X. Nonaqueous Liquid Electrolytes for Lithium-Based Rechargeable Batteries. *Chem. Rev.* **2004**, *104*, 4303–4417.
8. Mei, J.; Zhang, Y.; Liao, T.; Sun, Z.; Dou, S.X.; Chemistry, S.O. Strategies for improving the lithium-storage performance of 2D nanomaterials. *Natl. Sci. Rev.* **2018**, *5*, 389–416. [[CrossRef](#)]
9. Zahid, A.G.; Zhenhua, S.; Chengguo, S.; Fulai, Q.; Baigang, A.; Feng, L.; Hui, M.C. Key Aspects of Lithium Metal Anodes for Lithium Metal Batteries. *Small* **2019**, *15*, 1–26.
10. Cheng, C.F.; Xue, F.W.; Ying, S.M. Key Issues Hindering a Practical Lithium-Metal Anode. *Trend Chem.* **2019**, *26*, 1–7.
11. Chao, J.N.; Hong, K.L.; Shu, R.C.; Qiu, Y.L.; Jason, D.; Wu, X.; Ji, G.Z.; Whittingham, M.S.; Jie, X.; Jun, L. High-energy lithium metal pouch cells with limited anode swelling and long stable cycles. *Nat. Energy* **2019**, *4*, 551–559.
12. Peng, L.; Guo, Q.Z.; Xiao, B.; Zhen, G.; Xun, X.; Cheng, H.Y.; Wen, P.S.; Shi, X.D. Recent progress on silicon-based anode materials for practical lithium-ion battery applications. *Energy Storage Mater.* **2018**, *15*, 422–446.
13. Poizot, P.; Laruelle, S.; Grugeon, S.; Dupont, L.; Tarascon, J.M. Nano-sized transition-metal oxides as negative-electrode materials for lithium-ion batteries. *Nature* **2000**, *407*, 496–499. [[CrossRef](#)] [[PubMed](#)]
14. Abbas, S.M.; Hussain, S.T.; Ali, S.; Abbas, M.S. Structure and electrochemical performance of ZnO/CNT composite as anode material for lithium-ion batteries. *J. Mater. Sci.* **2013**, *48*, 5429–5436. [[CrossRef](#)]
15. Lu, S.; Wang, H.; Zhou, J.; Wu, X.; Qin, W. Atomic layer deposition of ZnO on carbon black as nanostructured anode materials for high-performance lithium-ion batteries. *Nanoscale* **2017**, *9*, 1184–1192. [[CrossRef](#)] [[PubMed](#)]
16. Hu, C.; Kirk, C.; Cai, Q.; Cuadrado-Collados, C.; Silvestre-Albero, J.; Rodríguez-Reinoso, F.; Biggs, M. A High-Volumetric-Capacity Cathode Based on Interconnected Close-Packed N-Doped Porous Carbon Nanospheres for Long-Life Lithium-Sulfur Batteries. *Adv. Energy Mater.* **2017**, *7*, 1701082. [[CrossRef](#)]
17. Courtel, F.M.; Duncan, H.; Abu-Lebdeh, Y.; Davidson, I.J. High capacity anode materials for Li-ion batteries based on spinel metal oxides AMn_2O_4 (A = Co, Ni, and Zn). *J. Mater. Chem.* **2011**, *21*, 10206–10218. [[CrossRef](#)]

18. Li, J.; Xiong, S.; Li, X.; Qian, Y. Spinel $Mn_{1.5}Co_{1.5}O_4$ core-shell microspheres as Li-ion battery anode materials with a long cycle life and high capacity. *J. Mater. Chem.* **2012**, *22*, 23254–23259. [[CrossRef](#)]
19. Hu, L.; Qu, B.; Li, C.; Chen, Y.; Mei, L.; Lei, D. Facile synthesis of uniform mesoporous $ZnCo_2O_4$ microspheres as a high-performance anode material for Li-ion batteries. *J. Mater. Chem. A* **2013**, *1*, 5596–5602. [[CrossRef](#)]
20. Reddy, M.V.; Rao, G.V.S.; Chowdari, B.V.R. Metal Oxides and Oxysalts as Anode Materials for Li Ion Batteries. *Chem. Rev.* **2013**, *113*, 5364–5457. [[CrossRef](#)]
21. Marka, S.K.; Petnikota, S.; Srikanth, V.V.S.S.; Reddy, M.V.; Stefan, A.; Chowdari, B.V.R. $Co_2Mo_3O_8$ /reduced graphene oxide composite: Synthesis, characterization, and its role as a prospective anode material in lithium ion batteries. *RSC Adv.* **2016**, *6*, 55167–55175. [[CrossRef](#)]
22. Das, B.; Reddy, M.V.; Krishnamoorthi, C.; Tripathy, S.; Mahendiran, R.; Rao, G.V.S.; Chowdari, B.V.R. Carbothermal synthesis, spectral and magnetic characterization and Li-cyclability of the Mo-cluster compounds, $LiYMo_3O_8$ and $Mn_2Mo_3O_8$. *Electrochim. Acta.* **2009**, *54*, 3360–3373. [[CrossRef](#)]
23. Das, B.; Reddy, M.V.; Tripathy, S.; Chowdari, B.V.R. A disc-like Mo-metal cluster compound, $Co_2Mo_3O_8$, as a high capacity anode for lithium ion batteries. *RSC Adv.* **2014**, *4*, 33883. [[CrossRef](#)]
24. Petnikota, S.; Marka, S.K.; Srikanth, V.V.S.S.; Reddy, M.V.; Chowdari, B.V.R. Elucidation of few layered graphene-complex metal oxide ($A_2Mo_3O_8$, A = Co, Mn and Zn) composites as robust anode materials in Li ion batteries. *Electrochim. Acta* **2015**, *178*, 699–708. [[CrossRef](#)]
25. Yuan, S.; Zhao, Y.; Chen, W.; Wu, C.; Wang, X.; Zhang, L.; Wang, Q. Self-assembled 3D hierarchical porous Bi_2MoO_6 microspheres toward high capacity and ultra-long-life anode material for Li-ion batteries. *ACS Appl. Mater. Interfaces* **2017**, *9*, 21781–21790. [[CrossRef](#)]
26. Zhai, X.; Gao, J.; Xue, R.; Xu, X.; Wang, L.; Tian, Q. Facile synthesis of Bi_2MoO_6 /reduced graphene oxide composites as anode materials towards enhanced lithium storage performance. *J. Colloid Interface Sci.* **2018**, *518*, 242–251. [[CrossRef](#)]
27. Kudin, T.I.T.; Zainal, N.F.A.; Ali, A.M.M. Electrochemical performance of anode material from palm oils derived carbon nanotubes for lithium ion batteries. *Mater. Res. Innov.* **2009**, *13*, 269–271. [[CrossRef](#)]
28. Wang, K.; Zhao, N.; Lei, S. Promising biomass-based activated carbons derived from willow catkins for high performance supercapacitors. *Electrochim. Acta.* **2015**, *166*, 1–11. [[CrossRef](#)]
29. Li, Y.; Trujillo, M.A.; Fu, E. Bismuth Oxide: A New Lithium-Ion Battery Anode. *J. Mater. Chem. A* **2013**, *1*, 12123–12127. [[CrossRef](#)]
30. Zhang, L.; Xu, T.; Zhao, X.; Zhu, Y. Controllable synthesis of Bi_2MoO_6 and effect of morphology and variation in local structure on photocatalytic activities. *Appl. Catal. B Environ.* **2010**, *98*, 138–146. [[CrossRef](#)]
31. Zheng, Y.; Zhou, T.; Zhao, X.; Pang, W.K.; Gao, H.; Li, S.; Zhou, Z.; Liu, H.; Guo, Z. Atomic interface engineering and electric-field effect in ultrathin Bi_2MoO_6 nanosheets for superior lithium ion storage. *Adv. Mater.* **2017**, *29*, 1700396. [[CrossRef](#)] [[PubMed](#)]
32. Kresse, G.; Furthmüller, J. Efficiency of ab-initio total energy calculations for metals and semiconductors using a plane-wave basis set. *Comput. Mater. Sci.* **1996**, *6*, 15–50. [[CrossRef](#)]
33. Kresse, G.; Hafner, J. Ab initio molecular dynamics for liquid metals. *Phys. Rev. B* **1993**, *47*, 558–561. [[CrossRef](#)] [[PubMed](#)]
34. Kresse, G.; Hafner, J. Ab initio molecular-dynamics simulation of the liquid-metal-amorphous-semiconductor transition in germanium. *Phys. Rev. B* **1994**, *49*, 14251–14269. [[CrossRef](#)] [[PubMed](#)]
35. Kresse, G.; Furthmüller, J. Efficient iterative schemes for ab initio total-energy calculations using a plane-wave basis set. *Phys. Rev. B. Condens. Matter.* **1996**, *54*, 11169–11186. [[CrossRef](#)] [[PubMed](#)]
36. Blöchl, P.E. Projector augmented-wave method. *Phys. Rev. B* **1994**, *50*, 17953. [[CrossRef](#)] [[PubMed](#)]
37. Monkhorst, H.J.; Pack, J.D. Special points for Brillouin-zone integrations. *Phys. Rev. B* **1976**, *13*, 5188–5192. [[CrossRef](#)]
38. Blöchl, P.E.; Jepsen, O.; Andersen, O.K. Improved tetrahedron method for Brillouin-zone integrations. *Phys. Rev. B* **1994**, *49*, 16223–16233. [[CrossRef](#)]
39. Perdew, J.; Burke, K.; Ernzerhof, M. Generalized gradient approximation made simple. *Phys. Rev. Lett.* **1996**, *77*, 3865–3868. [[CrossRef](#)]
40. Perdew, J.; Burke, K.; Ernzerhof, M. Errata: Generalized gradient approximation made simple. *Phys. Rev. Lett.* **1997**, *78*, 1396. [[CrossRef](#)]
41. Bader, R.F.W. *Atoms in Molecules: A Quantum Theory*; Oxford University Press: Oxford, UK, 1990.

42. Henkelman, G.; Arnaldsson, A.; Jónsson, H. A fast and robust algorithm for Bader decomposition of charge density. *Comput. Mater. Sci.* **2006**, *36*, 354–360. [[CrossRef](#)]
43. Geng, T.; Han, Z.; Zhuang, S. Effective Coulomb interaction in LaMnO₃. *Phys. B Condens. Matter.* **2010**, *405*, 3714–3716. [[CrossRef](#)]
44. Ravindran, P.; Kjekshus, A.; Fjellvåg, H.; Delin, A.; Eriksson, O. Ground-state and excited-state properties of LaMnO₃ from full-potential calculations. *Phys. Rev. B.* **2002**, *65*, 064445. [[CrossRef](#)]
45. Ravindran, P.; Vidya, R.; Fjellvåg, H.; Kjekshus, A. Electronic structure and excited-state properties of perovskite-like oxides. *J. Cryst. Growth.* **2004**, *268*, 554–559. [[CrossRef](#)]
46. Getsoian, A.; Shapovalov, V.; Bell, A.T. DFT+U investigation of propene oxidation over bismuth molybdate: Active sites, reaction intermediates, and the role of bismuth. *J. Phys. Chem. C* **2013**, *117*, 7123–7137. [[CrossRef](#)]
47. Dudarev, S.; Botton, G.; Savrasov, S. Electron-energy-loss spectra and the structural stability of nickel oxide: An LSDA+ U study. *Phys. Rev. B* **1998**, *57*, 1505–1509. [[CrossRef](#)]
48. Fan, X.; Zheng, W.T.; Kuo, J.L.; Singh, D.J. Adsorption of single Li and the formation of small Li clusters on graphene for the anode of lithium-ion batteries. *ACS Appl. Mater. Interfaces.* **2013**, *5*, 7793–7797. [[CrossRef](#)]
49. Amft, M.; Lebègue, S.; Eriksson, O.; Skorodumova, N.V. Adsorption of Cu, Ag, and Au atoms on graphene including van der Waals interactions. *J. Phys. Condens. Matter.* **2011**, *23*, 395001. [[CrossRef](#)]
50. Lee, S.; Lee, M.; Choi, H.; Yoo, D.S.; Chung, Y.C. Effect of nitrogen induced defects in Li dispersed graphene on hydrogen storage. *Int. J. Hydrogen Energy.* **2013**, *38*, 4611–4617. [[CrossRef](#)]
51. Grimme, S.; Ehrlich, S.; Goerigk, L. Effect of the damping function in dispersion corrected density functional theory. *J. Comput. Chem.* **2011**, *32*, 1456–1465. [[CrossRef](#)]
52. Yanovskii, V.K.; Voronkova, V.I. Polymorphism and properties of Bi₂WO₆ and Bi₂MoO₆. *Phys. Status Solidi.* **1986**, *93*, 57–66. [[CrossRef](#)]
53. Bi, J.; Wu, L.; Li, J.; Li, Z.; Wang, X.; Fu, X. Simple solvothermal routes to synthesize nanocrystalline Bi₂MoO₆ photocatalysts with different morphologies. *Acta Mater.* **2007**, *55*, 4699–4705. [[CrossRef](#)]
54. Yin, W.; Wang, W.; Sun, S. Photocatalytic degradation of phenol over cage-like Bi₂MoO₆ hollow spheres under visible-light irradiation. *Catal. Commun.* **2010**, *11*, 647–650. [[CrossRef](#)]
55. Huang, Y.; Li, K.; Li, S.; Lin, Y.; Liu, H.; Tong, Y. Ultrathin Bi₂MoO₆ nanosheets for photocatalysis: Performance enhancement by atomic interfacial engineering. *Chem. Select.* **2018**, *3*, 7423–7428.
56. Zhang, X.B.; Zhang, L.; Hu, J.S.; Huang, X.H. Facile hydrothermal synthesis and improved photocatalytic activities of Zn²⁺ doped Bi₂MoO₆ nanosheets. *RSC Adv.* **2016**, *6*, 32349–32357. [[CrossRef](#)]
57. Yang, Z.; Shen, M.; Dai, K.; Zhang, X.; Chen, H. Controllable synthesis of Bi₂MoO₆ nanosheets and their facet-dependent visible-light-driven photocatalytic activity. *Appl. Surf. Sci.* **2018**, *430*, 505–514. [[CrossRef](#)]
58. Murugan, R. Investigation on ionic conductivity and raman spectra of γ -Bi₂MoO₆. *Phys. B Condens. Matter.* **2004**, *352*, 227–232. [[CrossRef](#)]
59. Wu, J.-B.; Lin, M.-L.; Cong, X.; Liu, H.-N.; Tan, P.-H. Raman spectroscopy of graphene-based materials and its applications in related devices. *Chem. Soc. Rev.* **2018**, *47*, 1822–1873. [[CrossRef](#)]
60. Jiang, Z.; Jiang, Z.J.; Maiyalagan, T.; Manthiram, A. Cobalt oxide-coated N- and B-doped graphene hollow spheres as bifunctional electrocatalysts for oxygen reduction and oxygen evolution reactions. *J. Mater. Chem. A* **2016**, *4*, 5877–5889. [[CrossRef](#)]
61. Lan, L.; Shi, Z.; Zhang, Q.; Li, Y.; Yang, Y.; Wu, S.; Zhao, X. Defects lead to a massive enhancement in the UV-Vis-IR driven thermocatalytic activity of Co₃O₄ mesoporous nanorods. *J. Mater. Chem. A* **2018**, *6*, 7194–7205. [[CrossRef](#)]
62. Fang, J.; Yuan, Y.F.; Wang, L.K.; Ni, H.L.; Zhu, H.L.; Yang, J.L. Synthesis and electrochemical performances of ZnO/MnO₂ sea urchin-like sleeve array as anode materials for lithium-ion batteries. *Electrochim. Acta* **2009**, *112*, 364–370. [[CrossRef](#)]
63. Lu, Y.; Wang, L.; Preuß, K.; Qiao, M.; Titirici, M.-M.; Varcoe, J.; Cai, Q. Halloysite-derived nitrogen doped carbon electrocatalysts for anion exchange membrane fuel cells. *J. Power Sources* **2017**, *372*, 82–90. [[CrossRef](#)]
64. Zhang, R.H.; Zhao, T.S.; Tan, P.; Wu, M.C.; Jiang, H.R. Ruthenium dioxide-decorated carbonized tubular polypyrrole as a bifunctional catalyst for non-aqueous lithium-oxygen batteries. *Electrochim. Acta* **2017**, *257*, 281–289. [[CrossRef](#)]
65. Kwon, K.C.; Song, M.J.; Kwon, K.H.; Jeoung, H.V.; Kim, D.W.; Lee, G.S.; Hong, J.P.; Park, J.G. Nanoscale CuO solid-electrolyte-based conductive-bridging-random-access-memory cell operating multi-level-cell and 1selector1resistor. *J. Mater. Chem. C* **2015**, *3*, 9540–9550. [[CrossRef](#)]

66. Wippermann, K.; Giffin, J.; Kuhri, S.; Lehnert, W.; Korte, C. The influence of water content in a proton-conducting ionic liquid on the double layer properties of the Pt/PIL interface. *Phys. Chem. Chem. Phys.* **2017**, *19*, 24706–24723. [[CrossRef](#)] [[PubMed](#)]
67. Yu, B.; Yu, H.; Huang, T.; Wang, H.; Zhu, M. A biomimetic nanofiber-based triboelectric nanogenerator with an ultrahigh transfer charge density. *Nano Energy* **2018**, *48*, 464–470. [[CrossRef](#)]
68. Boukamp, B.A. Derivation of a Distribution Function of relaxation times for the (fractal) finite length Warburg. *Electrochim. Acta* **2017**, *252*, 154–163. [[CrossRef](#)]
69. Hayamizu, K. Direct relations between ion diffusion constants and ionic conductivity for lithium electrolyte solutions. *Electrochim. Acta.* **2017**, *254*, 101–111. [[CrossRef](#)]
70. Billaud, J.; Eames, C.; Tapia-Ruiz, N.; Roberts, M.R.; Naylor, A.J.; Armstrong, A.R.; Islam, M.S.; Bruce, P.G. Evidence of enhanced ion transport in Li-rich silicate intercalation materials. *Adv. Energy Mater.* **2017**, *7*, 1–9. [[CrossRef](#)]
71. Li, Q.; Liu, H.; Yao, Z.; Cheng, J.; Li, T.; Li, Y.; Wolverton, C.; Wu, J.; Dravid, V.P. Electrochemistry of selenium with sodium and lithium: Kinetics and reaction mechanism. *ACS Nano* **2016**, *10*, 8788–8795. [[CrossRef](#)]
72. Islam, M.S.; Fisher, C.A.J. Lithium and sodium battery cathode materials: Computational insights into voltage, diffusion and nanostructural properties. *Chem. Soc. Rev.* **2014**, *43*, 185–204. [[CrossRef](#)] [[PubMed](#)]
73. Zhang, S.; Northrup, J. Chemical potential dependence of defect formation energies in GaAs: Application to Ga self-diffusion. *Phys. Rev. Lett.* **1991**, *67*, 2339–2342. [[CrossRef](#)]
74. Grau-Crespo, R.; Hamad, S.; Catlow, C.R.A.; De Leeuw, N.H. Symmetry-adapted configurational modelling of fractional site occupancy in solids. *J. Phys. Condens. Matter.* **2007**, *19*, 256201. [[CrossRef](#)]
75. Olsson, E.; Chai, G.; Dove, M.; Cai, Q. Adsorption and migration of alkali metals (Li, Na, and K) on pristine and defective graphene surfaces. *Nanoscale.* **2019**, *11*, 5274–5284. [[CrossRef](#)] [[PubMed](#)]
76. Heath, J.; Chen, H.; Islam, M.S. MgFeSiO₄ as a potential cathode material for magnesium batteries: Ion diffusion rates and voltage trends. *J. Mater. Chem. A.* **2017**, *5*, 13161–13167. [[CrossRef](#)]
77. Eames, C.; Armstrong, A.R.; Bruce, P.G.; Islam, M.S. Insights into changes in voltage and structure of Li₂FeSiO₄ polymorphs for lithium-ion batterie. *Chem. Mater.* **2012**, *24*, 2155–2161.
78. Aparicio, P.A.; Dawson, J.A.; Islam, M.S.; De Leeuw, N.H. Computational study of NaVOPO₄ polymorphs as cathode materials for Na-ion batteries: Diffusion, electronic properties, and cation-doping behavior. *J. Phys. Chem. C* **2018**, *122*, 25829–25836.
79. Aydinol, M.; Kohan, A.; Ceder, G.; Cho, K.; Joannopoulos, J. Ab initio study of lithium intercalation in metal oxides and metal dichalcogenides. *Phys. Rev. B Condens Matter Mater. Phys.* **1997**, *56*, 1354–1365. [[CrossRef](#)]
80. Arroyo-de Dompablo, M.E.; Armand, M.; Tarascon, J.M.; Amador, U. On-demand design of polyoxianionic cathode materials based on electronegativity correlations: An exploration of the Li₂MSiO₄ system (M = Fe, Mn, Co, Ni). *Electrochem. Commun.* **2006**, *8*, 1292–1298. [[CrossRef](#)]
81. Armstrong, A.R.; Lyness, C.; Panchmatia, P.M.; Islam, M.S.; Bruce, P.G. The lithium intercalation process in the low-voltage lithium battery anode Li_{1+x}V_{1-x}O₂. *Nat. Mater.* **2011**, *10*, 223–229. [[CrossRef](#)]
82. Liu, M.; Rong, Z.; Malik, R.; Canepa, P.; Jain, A.; Ceder, G.; Persson, K.A. Spinel compounds as multivalent battery cathodes: A systematic evaluation based on ab initio calculations. *Energy Environ. Sci.* **2015**, *8*, 964–974. [[CrossRef](#)]

